Computational Materials Science 231 (2024) 112542

Contents lists available at ScienceDirect

Computational Materials Science

journal homepage: www.elsevier.com/locate/commatsci

Efficient ab initio stacking fault energy mapping for dilute interstitial alloys

Frank Niessen [a,*], Konstantin V. Werner [a], Wei Li [b,c], Song Lu [b], Levente Vitos [b,c,d], Matteo Villa [a], Marcel A.J. Somers [a]

[a] *Department of Civil and Mechanical Engineering, Technical University of Denmark, 2800 Kgs. Lyngby, Denmark*
[b] *Applied Materials Physics, Department of Materials Science and Engineering, Royal Institute of Technology, Stockholm SE-100 44, Sweden*
[c] *Department of Physics and Astronomy, Division of Materials Theory, Uppsala University, P.O. Box 516, SE-75121 Uppsala, Sweden*
[d] *Research Institute for Solid State Physics and Optics, Wigner Research Center for Physics, P.O. Box 49, H-1525 Budapest, Hungary*

ABSTRACT

Density Functional Theory (DFT) is the prevalent first principles computational method for determining the stacking fault energy (SFE) of face centered cubic (*fcc*) metals and alloys. Due to several theoretical and computational challenges, SFE determination for interstitial alloys with alloying elements such as carbon, nitrogen, and hydrogen, has so far been limited to few studies at relatively high interstitial content. We propose a new method, rooted in the axial interaction model, that allows rapid and robust mapping of SFE for virtually arbitrary interstitial contents. Instead of computing the total energy of a very large supercell to represent dilute interstitial solutions, representative interstitial-affected and bulk regions are treated separately at the equivalent volume. The SFE is obtained by balancing the SFE values of the regions with a lever rule approach. The method matches SFE values from the axial interaction model within ≤ 4 mJ.m^{-2} error, as validated for non-magnetic *fcc* Fe-N and paramagnetic *fcc* Fe-N and AISI 304 alloys. The significantly reduced computational workload and equidistant SFE mapping vs. interstitial content down to extremely low values allows accurate fitting of the SFE vs. interstitial content with only few datapoints. This further improves the computational efficiency. So far DFT-based SFE mapping was limited to purely substitutional alloys; we demonstrate the first-time DFT-based SFE mapping in *fcc* AISI 304 vs. N and Ni, revealing a non-additive contribution of N and Ni to the SFE. Finally, the remaining challenges and future application for high-throughput DFT SFE computation in interstitial alloys is discussed.

1. Introduction

The stacking fault energy (SFE) is the energy associated with a stacking fault in-between two Shockley partial dislocations following the dissociation of a full dislocation. In face-centered-cubic (*fcc*) alloys, SFE is used as a parameter to delineate the different predominant plastic deformation mechanisms. At a given pressure and temperature, the SFE of alloys can be altered by changing the chemical composition [1,2]. For increasing SFE, the prevalent deformation mechanism changes from martensite formation to twinning to, exclusively, dislocation slip [3,4]. Given the pivotal technological relevance of interstitial elements in modern alloy design [5–9], their effect on SFE is a prominent area of research.

Attempts to estimate SFE values computationally can be made with thermodynamic modelling techniques such as CALPHAD [10,11] and Density Functional Theory (DFT) [12,13]. CALPHAD is the preferred method for the efficient computation of phase equilibria as a function of temperature, pressure, and alloy composition. Being able to compute the Gibbs energies of the hexagonal-closed-packed (*hcp*) and *fcc* lattices of complex interstitial-containing multicomponent alloys, the method principally lends itself well to mapping the SFE vs. composition. However, the Gibbs energies at low temperatures, especially for metastable phases with an *hcp* lattice in steel [14], are inaccurate in thermodynamics databases, leading to unacceptable uncertainties [15,16]. This shortcoming is commonly addressed by selectively compiling [4,16–19] or fitting [4] thermodynamics parameters to improve the agreement between CALPHAD-computed SFE values and experimentally determined SFE values. This practice seems insensible given the recent realization that experimentally determined SFE values include unaccounted for kinetics contributions to form stacking faults, in addition to the thermodynamics associated with the presence of a stacking fault [20–24].

DFT modeling has become an established approach for the determination of SFE values for metals and alloys [2,25–28]. While its capability to determine SFE of interstitial alloys has been successfully demonstrated [25,27,29–32], up to now only little work has been performed in comparison to interstitial-free alloys. Several limitations of current DFT approaches for SFE determination complicate its application for large-scale SFE mapping in interstitial alloys:

---

* Corresponding author.
E-mail address: frannie@dtu.dk (F. Niessen).

https://doi.org/10.1016/j.commatsci.2023.112542
Received 6 July 2023; Received in revised form 27 September 2023; Accepted 27 September 2023
Available online 6 October 2023
0927-0256/© 2023 The Author(s). Published by Elsevier B.V. This is an open access article under the CC BY license (http://creativecommons.org/licenses/by/4.0/).

(i) Explicit modeling of a stacking fault within a supercell is commonly considered to be the most accurate way of modeling the SFE, as the interaction between solute and the stacking fault and the interfacial energy are explicitly accounted for. For alloys containing interstitials, the position of the interstitial atom relative to the stacking fault has an immense effect on the obtained SFE values [25,31]. So far, the general tendency of interstitial segregation to stacking faults has been proven experimentally [32,33], but the precise planar distribution of interstitial atoms adjacent to the stacking fault has remained undetermined, even using the most recent high-resolution materials characterization methods [33]. Hence, choosing a reasonable assumption for modeling the SFE to predict the deformation behavior is complicated.

As an alternative to explicit modeling of the stacking fault, the less detailed first-order term of the axial interaction model [2,34,35] may be applied, in which the total energies of separate *fcc* and *hcp* supercells are evaluated without explicit modeling of the stacking fault. The obtained values were shown to agree with mean values of explicitly determined SFE values at different interstitial positions [25,31]. While this approach could be deemed less accurate, it is an efficient and robust approach to map the overall influence of composition on SFE.

(ii) Interstitial contents in technologically relevant alloys are commonly lower than 0.1 wt% [36–39]. Calculation of the SFE of alloys with low interstitial content with DFT would require extremely large supercells that are associated with an infeasible computational workload and complicated convergence. To determine the SFE of a Fe-0.05C (wt.%) alloy for instance, a single carbon atom would need to be dissolved into a massive supercell of 432 host-lattice Fe atoms. Moreover, local distortions in the host lattice that are introduced by the interstitial atom causes the breakdown of crystal symmetry, leading to further computational workload. For most dilute interstitial alloys, SFE mapping is therefore unfeasible.

(iii) Not all DFT formalisms support optimization-guided ionic relaxation. Manually redefining the atomic positions in the supercells around the interstitial site is tedious and can only be carried out approximately. As DFT studies often concern mapping of a property as a function of systematically changed parameters, the validity of the determined local relaxation must be assumed or proven valid within the mapped parameter interval. This complication does not only concern the local relaxation around the interstitial atom, but also all other ionic and cell relaxations such as the c/a-ratio in *hcp* supercells.

(iv) Many technologically important interstitial alloys, such as austenitic stainless steels, are in a paramagnetic state at ambient temperature, albeit rarely accounted for in DFT calculations [29,31,40]. In DFT formalisms that incorporate the coherent potential approximation (CPA) [41,42], the paramagnetic state can partially be accounted for by applying the disordered local magnetic moment method [43]. Alternatively, Dick et al. [29] demonstrated treatment of paramagnetic properties in Fe-C by averaging over several supercells with randomly initialized magnetic moments. This approach gave excellent agreement with results obtained by the disordered local magnetic moment method [31]. However, it is computationally inefficient and may not be directly transferable to substitutional alloys that contain multiple species per sublattice.

In summary, CALPHAD modeling is the preferred method for SFE mapping across large interstitial compositional spaces, but it currently lacks the required accuracy for reliable SFE prediction due to inaccurate CALPHAD databases for the phases and temperature ranges of interest. DFT on the other hand yields physically meaningful SFE values, but for SFE mapping of interstitial alloys the method is too involved and computationally expensive. Not surprisingly, recent research therefore focusses on creating new, third generation CALPHAD databases, that are accurate down to 0 K even for metastable phases [14,15,44,45]. These databases are not, as traditionally, exclusively built on experimental data but informed by DFT calculations.

With this motivation, the present work proposes a new DFT-based method that attempts to drastically reduce the required computational resources to enable SFE mapping in dilute interstitial alloys. The method circumvents the necessity of computing the total energies of extremely large supercells to reduce the use of computational resources and to enable the assessment of systems with extremely low interstitial contents. The method is successfully validated against SFE results from the axial interaction model for the *fcc* Fe-N system and nitrogen alloyed AISI 304 austenitic stainless steel and is applied to demonstrate its potential for large-scale SFE mapping.

2. Ab initio methods

All calculations in this work were carried out using the CPA [41,42] as implemented in the exact muffin-tin orbitals (EMTO) package [42,46]. The paramagnetic state was accounted for using the disordered local magnetic moment (DLM) method [43]. In the calculations, the radii of the Wigner-Seitz spheres of nitrogen were optimized, leading to a reduction of 23% compared to the host-lattice elements. For nitrogen, $2p$ and $2s^2$ were considered as valence states. The k-point density in each supercell was optimized to yield an error in SFE < 0.01 mJ.m^{-2}.

To partially account for the finite temperature effect, experimental relationships for the *fcc* lattice parameters as a function of nitrogen were adopted for the atomic volumes. Further details on the optimization of the c/a ratio of the *hcp* supercells, the general layout of the supercells, the strategy for relaxing the first coordination shell and the validation of the chosen configuration with literature data are reported elsewhere [40].

The self-consistent EMTO(CPA) Green's function calculations were carried out using all 40 cores of Intel® Xeon® Scalable Gold CPU 6148 @ 2.20 GHz Skylake nodes, whereas the less involved determination of the total energy functional from the full charge density was carried out using the single cores of an Intel® Core™ i9-10920X CPU @ 3.50 GHz node. The stated runtimes in this manuscript are indicative, as they strongly depend on various freely adjustable parameters to steer the convergence of the self-consistent routine. It was attempted to optimize these parameters towards maximum performance.

3. The lever rule approach

3.1. SFE model

For the lever rule approach, the intrinsic SFE, γ, is approximated using the first-order term of the axial interaction model [2,34,35]:

$$\gamma = 2(F_{hcp} - F_{fcc})/A \tag{1}$$

where F_{hcp} and F_{fcc} are the atomic Helmholtz energies of the *hcp* and *fcc* lattices, and A is the area of the stacking fault per atom. Abbasi et al. [25] and Lu et al. [31] obtained SFE values for *fcc* Fe-C in agreement with averaged SFE values from supercells with carbon atoms placed at different offsets with respect to the stacking fault. The axial interaction model is insensitive to local interactions of interstitials with the interface. It also neglects the interfacial energy, as the stacking fault is not modelled explicitly. The strain field of the partial dislocations is always neglected in DFT modeling, as even explicitly modelled stacking faults within supercells extend infinitely across the periodic boundary conditions. Adding an interfacial energy term to Eq. (1), it becomes equivalent to the Olson-Cohen model [14]. F_{hcp} and F_{fcc} were determined from two individual *hcp* and *fcc* supercells without explicit modeling of the stacking fault. The Helmholtz energy of each phase consists of the total energy, E_{tot}, and, optionally, of the magnetic entropy, F_{mag}, at experimentally determined atomic volumes, $V(T)$:

$$F(V,T) = E_{tot}(V(T)) + F_{mag}(\mu_i(V(T)),T) \tag{2}$$

F_{mag} is a function of T and the local magnetic moments μ_i of the atoms at lattice site i and was approximated by a mean field expression which is valid for completely disordered localized moments [47]:

$$F_{mag} = -TS_{mag} = -k_B T \sum_i \ln(1+\mu_i(V(T))) \tag{3}$$

where k_B is Boltzmann's constant.

3.2. Concept

The lever rule approach for SFE determination in dilute interstitial alloys is introduced via an example before introducing the generalization in Section 3.3. Fig. 1 shows Fe *hcp* and *fcc* supercells in which a single nitrogen atom resides in an octahedrally coordinated interstice. The $Fe_{32}N_1$ (Fig. 1a and b) and $Fe_{64}N_1$ (Fig. 1c) supercells are associated with interstitial contents of 0.78 and 0.39 wt% nitrogen, respectively. The first coordination shell (shown in green) is relaxed around the interstitial atom (shown in red) to account for interstitially induced lattice distortion. More detail on the generation of these supercells is given in Ref. [40] and the SFE values associated with these supercells are obtained via Equation (1).

The supercell for $Fe_{64}N_1$ in Fig. 1c was visually divided into an interstitial-affected region and a bulk region. The lever rule approach is based on the hypothesis that atoms in the bulk region are sufficiently remote from the interstitial atom so they do not experience the alloying effect of the interstitial atom in their total energy. Provided that this hypothesis holds, the total energy of the $Fe_{64}N_1$ supercell in Fig. 1c can be divided into two contributions: the total energy of a $Fe_{32}N_1$ supercell, representing the interstitial region, and a Fe_{32} supercell, representing the bulk region. As Eq. (1) for the SFE is based on the difference in total energy between the *hcp* and *fcc* lattices, the SFE of the $Fe_{64}N_1$ supercell can be directly described by the mean value of the SFE values for the $Fe_{32}N_1$ and Fe_{32} supercells, weighted by their respective number of atoms. Furthermore, the total energy per atom of the Fe_{32} supercell is, within marginal numeric error, identical to the total energy of a primitive cell of Fe [40]. Therefore, assuming a negligible error from dividing the $Fe_{64}N_1$ supercell into interstitial-affected and bulk regions, the lever rule allows SFE calculation for $Fe_{64}N_1$ by computing the SFE values of $Fe_{32}N_1$ and Fe.

3.3. Generalization, scope and limitations

The lever rule approach aims at determining the intrinsic SFE of the supercell ,γ_s, with n_S atoms and volume V_s. The supercell contains one interstitial atom per $n_S - 1$ host atoms to reflect the interstitial occupancy $y_s = (n_S - 1)^{-1}$. The occupancy thus describes the number of interstitial atoms per host atom. The lever rule approximates γ_s in terms of the weighted average between the SFE of the interstitial region γ_i and the bulk region γ_b. The interstitial region consists of one interstitial atom per $n_i - 1$ host atoms to reflect the interstitial occupancy $y_i = (n_i - 1)^{-1}$ and the weights applied to γ_i and γ_b reflect the molar fraction of the interstitial region with respect to the total supercell:

$$\begin{aligned}\gamma_s(y_s, y_i, V_s) &= \frac{n_i}{n_s}\gamma_i(V_s) + \left(1 - \frac{n_i}{n_s}\right)\gamma_b(V_s) \\ &= \frac{{y_i}^{-1}+1}{{y_s}^{-1}+1}\gamma_i(V_s) + \left(1 - \frac{{y_i}^{-1}+1}{{y_s}^{-1}+1}\right)\gamma_b(V_s)\end{aligned} \tag{4}$$

While the lever rule approach in principle describes a simple linear relation between γ_s and the interstitial occupancy y_s by balancing the two SFE values γ_i and γ_b, consideration of the interstitially-induced change in the super cell volume V_s introduces a non-linear component to Eq. (4). Employing the CPA within the here applied EMTO formulation allows the analysis of virtually any randomized alloy composition. The maximum interstitial occupancy y^s_{max} that can be treated with the lever rule approach is given by $y^s_{max} = (n_i - 1)^{-1}$. A larger value for n_i, i.e. a larger interstitial region, reduces y^s_{max}. A larger interstitial region should however also improve the accuracy of the method, as more of the energy tails from interstitial alloying are accounted for. We will demonstrate in the following section that this comes at the expense of additional required computational resources.

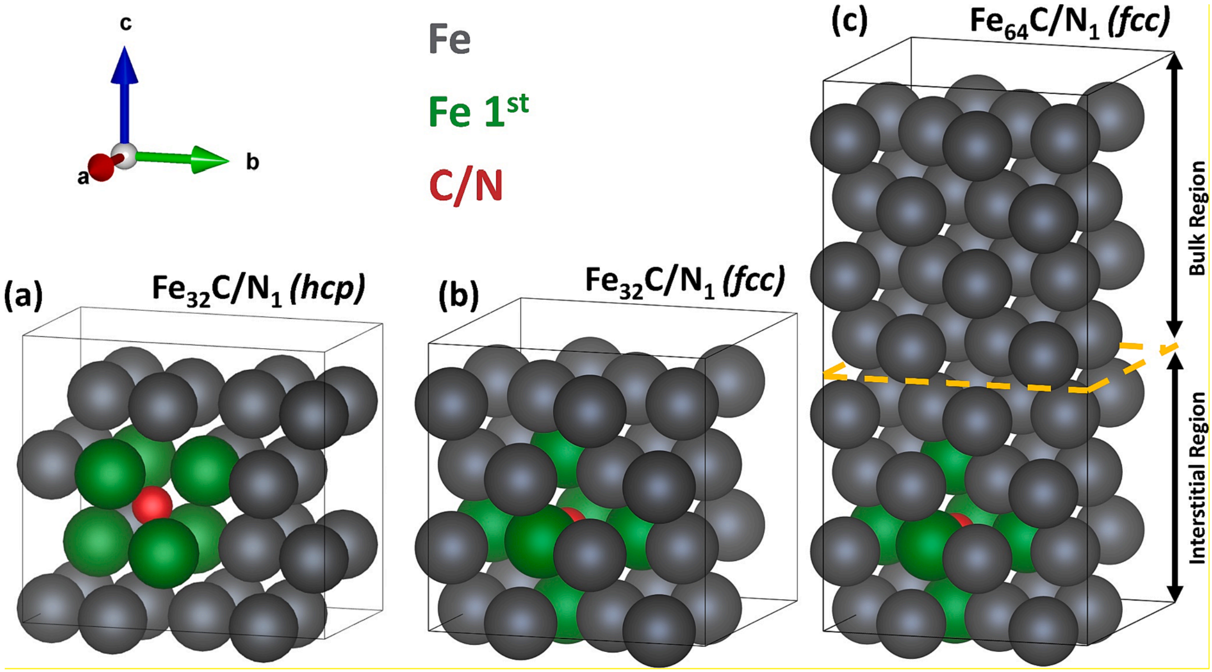

Fig. 1. (a) hcp $Fe_{32}N_1$, (b) fcc $Fe_{32}N_1$ and (c) fcc $Fe_{64}N_1$ supercells. Fe atoms are colored in gray, the N (interstitial) atom is colored in red, and Fe atoms in the 1st coordination shell to N are colored in green. Panel (c) indicates the interstitial-affected and bulk regions.

A critical assumption of the method is that the host composition of the substitutional crystal lattice can be accurately described by a supercell with $n_i - 1$ atoms. The method is therefore ideal for treating single-species host lattices (such as *fcc* Fe-N) or random complex alloys when combined with the CPA. Compositional randomness on the host lattice may alternatively be represented by computing Special Quasi-random Structure [48] or Small Set of Ordered Structures [49] with $n_i - 1$ host atoms, which will not be explored further in this work.

3.4. *Validation*

The idea that supercells for dilute interstitial alloys can be divided into an interstitial-affected region and a bulk region is intuitive, in particular for extremely large supercells. The hypothesis nevertheless requires thorough validation to determine relevant limitations and error estimates. The main source of validation is the comparison of SFE values obtained from the lever rule approach in Eq. (4) with SFE values that are directly obtained from the axial interaction model in Eq. (1).

3.4.1. *Non-magnetic fcc Fe-N*

The lever rule approach is first validated for the relationship between SFE and nitrogen occupancy for non-magnetic austenitic (*fcc*) Fe-N. For the interstitial regions, two sets of calculations are performed in which a single nitrogen atom is inserted in cells of $n_i - 1 = 32$ and 48 host atoms. The SFE values γ_i and γ_b are computed for each atomic volume associated with the different overall nitrogen occupancies V_s which is given by the experimentally determined relationship reported by Cheng et al. [50]:

$$a_0^s\left(y_N^s\right) = 3.573 + 0.0072\, y_N^s\ [\text{Å}] \tag{5}$$

where y_N^s is the nitrogen occupancy and a_0^s is the *fcc* lattice parameter of the entire supercell. The c/a-ratio of 1.594 was obtained by relaxing the $Fe_{32}N_1$ *hcp* cell at the ground-state volume and was kept constant for all following calculations. The dependence of SFE on nitrogen content in non-magnetic *fcc* Fe-N was previously assessed with DFT modeling by Kibey et al. [51] and Niessen et al. [40]. The latter reference shows that the obtained SFE vs. nitrogen occupancy relationship is linear and equivalent to the SFE vs. carbon occupancy relationship, previously treated by Abbasi et al. [25], Gholizadeh et al. [52], Medvedeva et al. [27] and Lu et al. [31]. Fig. 2 shows the SFE values obtained from the lever rule approach considering interstitial regions of $n_i = 33$ and 49 atoms. The data is compared with SFE values from direct application of the axial interaction model in Eq. (1) with supercells containing 32, 48, 64 and 80 host atoms. These values are in excellent agreement with the SFE values from the lever rule approach. $\Delta\gamma_s$ shows the deviation of all data points from the linear fit γ_s = -35352 + 9786 a_0^s [mJ.m^{-2}] to the validation dataset. It is apparent that both data series from the lever rule approach fall within the standard error of the linear fit, i.e. $\leq$3 mJ.m^{-2}. The lever rule approach was also used to compute SFE values for even larger supercells, $Fe_{96}N_1$ and $Fe_{112}N_1$.

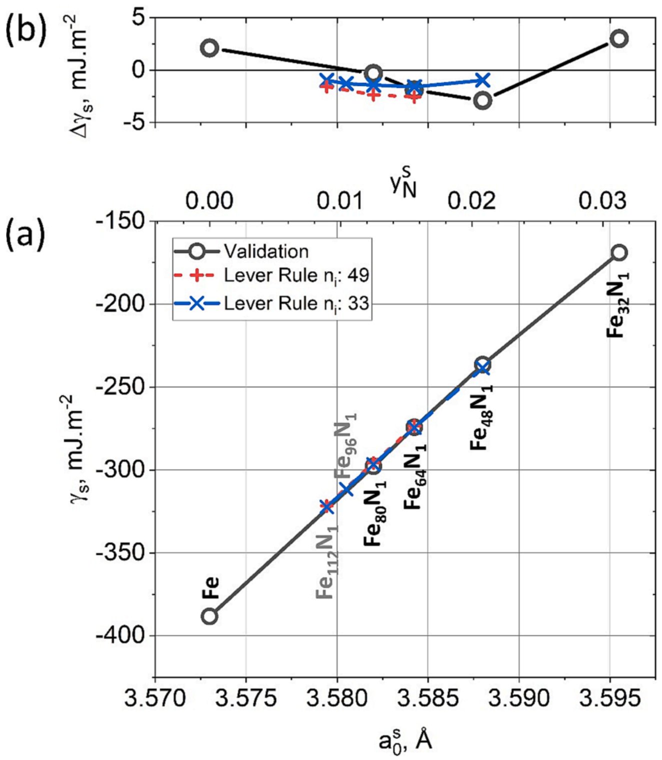

Fig. 2. (a) SFE (γ_s) of non-magnetic Fe-N as a function of lattice parameter a_0^s and nitrogen occupancy y_N^s. Both SFE values from the lever rule using $n_i = 33$ and $n_i = 49$ are in excellent agreement with the validation dataset of SFE obtained from applying Eq. (1) to the entire supercell. $\Delta\gamma_s$ in panel (b) indicates the discrepancy between all data points with respect to a linear fit of the validation dataset.

The runtime of total energy calculations required for the different approaches for SFE determination in Fig. 2 is compared in Fig. 3. As expected, for conventional SFE calculation following the axial interaction model, the runtime increases gradually with reduced interstitial content, associated with increased supercell size, whereas the computational resources required for the lever rule approach are independent of the interstitial content. The runtimes for the overall approaches applied to the highlighted five supercells are 10.2 ks (~2.8 h) for n_i = 33, 23.0 ks (~6.4 h) for n_i = 49, and 30.4 ks (~8.4 h) for the conventional axial interaction model. These overall runtimes take into account that only supercells with less than n_i atoms can be treated with the lever rule approach, while the remaining supercells are treated with the conventional approach (as indicated by the dashed lines in Fig. 3). While for n_i = 33 about 2/3 of the computational resources is saved with respect to conventional SFE determination, for n_i = 49 the reduction in computational resources is only ~1/4. The performance gain using the lever rule approach will significantly increase when considering even larger supercells, i.e. more diluted interstitial solutions, and when treating more complex systems that are more difficult to converge.

3.4.2. *Paramagnetic fcc Fe-N*

Next, the complexity of the calculations is enhanced by considering paramagnetic properties for the *fcc* Fe-N alloy. The conditions for the atomic volume at ambient temperature and the c/a-ratio of the *hcp* lattice were kept identical to the non-magnetic case described in the previous section. Fig. 4 shows the difference in total energy ΔE_{tot} for the *fcc* and *hcp* cells of the bulk (*b*) and interstitial regions (i) with $n_i = 33$ at different *fcc* lattice parameters a_0^s and nitrogen occupancies y_N^s of the entire supercell. The total energies for *fcc* and *hcp* in the bulk region are close to each other and for low volume or nitrogen occupancy the *hcp* crystal structure is favored over the *fcc* crystal structure. From y_N^s = 0.009 the *fcc* crystal structure becomes stable in the bulk region. The interstitial region on the other hand consistently favors *fcc* over *hcp*. The resulting SFE values γ_s and γ_i as determined with Eq. (1) are shown on the right y-axis as a function of volume and y_N. For clarity, the SFE values are here obtained directly from ΔE_{tot}^b and ΔE_{tot}^i, i.e., the magnetic entropy contribution is not included.

To obtain direct validation of the assumption of an interstitial-affected region and a bulk region within the supercell, the local atomic energies are plotted for paramagnetic *fcc* $Fe_{64}N_1$ (supercell in Fig. 1c). Fig. 5 shows the supercell with Fe atoms colored according to their site-projected energy with respect to the lowest site-projected energy value; the position of nitrogen is indicated with a black pentagram marker. The site projected energy is defined using the site-projected density of states for the one electron energy contribution plus the intracell, local exchange–correlation and site-projected Madelung

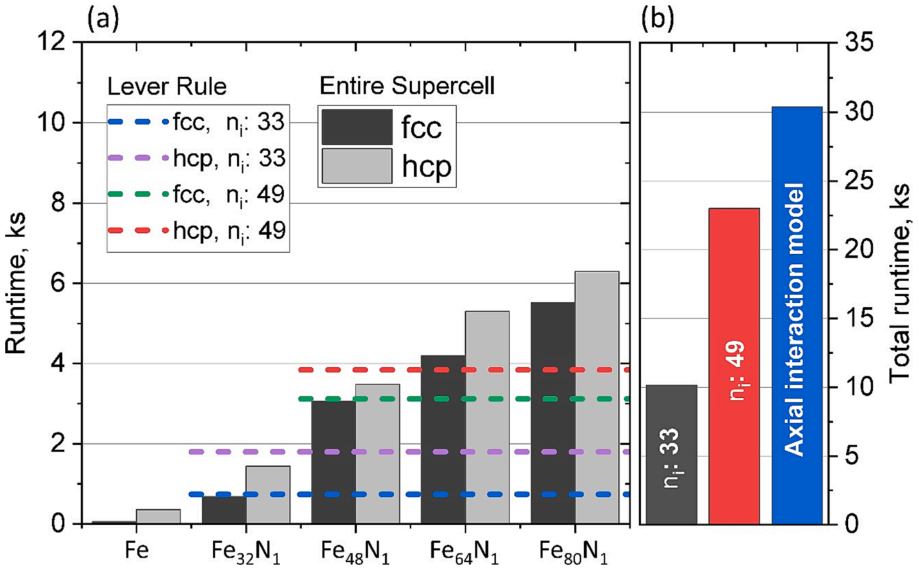

Fig. 3. (a) Runtime of the total energy calculations of the entire fcc and hcp supercells (grey bars) vs. the average runtime using the lever rule approach with $n_i = 33$ and $n_i = 49$. The total runtime for the 5 considered supercells in panel (b) shows that the lever rule approach saves ~2/3 of computational resources for $n_i = 33$ and ~1/4 of computational resources for $n_i = 49$.

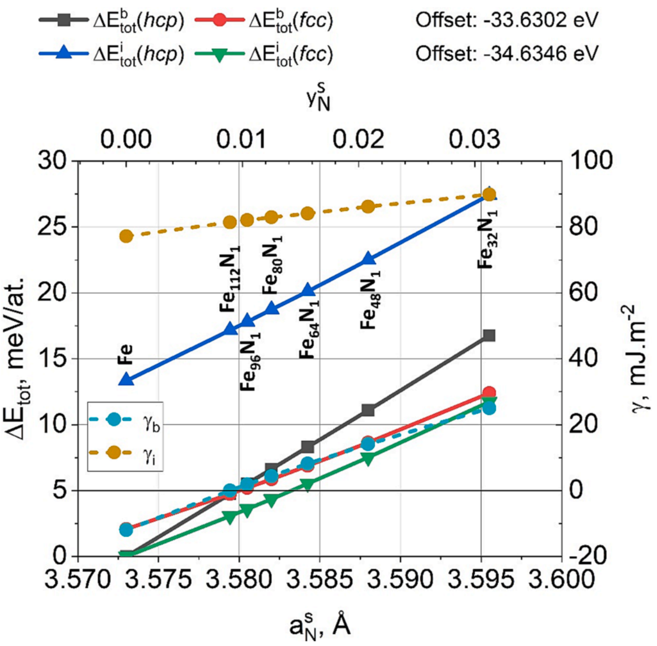

Fig. 4. Relative total energies of the fcc and hcp supercells of the bulk (ΔE^b_{tot}) and interstitial (ΔE^i_{tot}) regions at different volumes and corresponding nitrogen occupancies of the entire supercell. Using Eq. (1) the associated SFE values γ_b and γ_i of the two regions are determined (here shown without the magnetic entropy contribution). The bulk region is metastable at the interstitial-free volume of whereas the interstitial region is stable throughout the entire volume range.

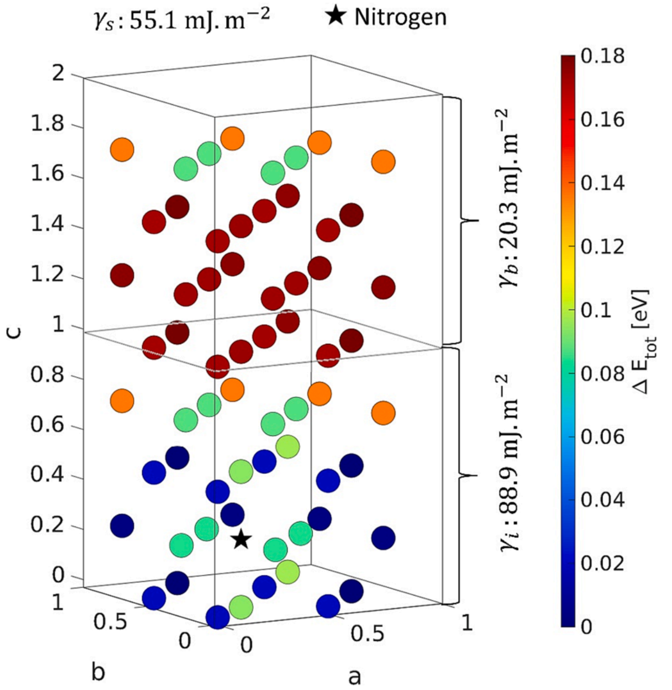

Fig. 5. Site projected energies with respect to the lowest site projected energy value in the $Fe_{64}N_1$ paramagnetic supercell. The entire supercell is separated into a bulk region and an interstitial-affected region. Fe atoms that are near nitrogen (black pentagram marker) are associated with a relatively reduced total energy.

contributions. The uppermost 32 atoms are considered the bulk region. Indeed, the atoms in this region show approximately constant atomic energy, as indicative of a homogeneous, defect-free bulk lattice. Only the uppermost row shows reduced atomic energies that are associated with the alloying effect of nitrogen across the periodic boundary along the *c*-axis of the supercell. The interstitial region in Fig. 5 shows, as expected, a drastic reduction in energy for the atoms that are close to nitrogen. The data clearly supports the hypothesis of a bulk and an interstitial-affected region, despite the slight inhomogeneity introduced in the bulk region across the periodic boundary. The following convincing validation of the obtained SFE values will show that the introduced error by these unaccounted energy tails is negligible. For the present case, it is anticipated that an interstitial region consisting of 48 host atoms, i.e. ¾ of the present supercell volume, should give a slightly more accurate representation of the regional energies.

Fig. 5 also states the SFE values that are associated with the different regions (including the contribution of the magnetic entropy F_{mag}). It is evident that interstitial alloying in the interstitial region leads to a drastic increase in SFE with respect to the interstitial-free bulk region, and that the SFE value for the entire supercell is given by a mixed contribution from both subregions. Applying Equation (4) consequently yields: $\gamma_s\left(y_s = \frac{1}{65}\right) = 88.9\mathrm{mJ.m}^{-2}\left(\frac{33}{65}\right) + 20.3\mathrm{mJ.m}^{-2}\left(1 - \frac{33}{65}\right) = 55.1\mathrm{mJ.m}^{-2}$. The SFE value following the axial interaction model in Equation (1) yields 57.5 $\mathrm{mJ.m}^{-2}$. The error from an imperfect separation of the interstitial-affected and bulk regions thus only amounts to $\leq$2.4 $\mathrm{mJ.m}^{-2}$.

Fig. 6 shows the SFE obtained from the lever rule in direct comparison with the validation data obtained from the axial interaction model for different nitrogen contents and atomic volumes [40]. Assuming an interstitial region of $n_i = 33$, the introduced error is $\leq$3.5 $\mathrm{mJ.m}^{-2}$. For a larger interstitial region of $n_i = 49$, this error is further reduced to $\leq$0.8 $\mathrm{mJ.m}^{-2}$, as anticipated from the distribution of the site-projected energies in Fig. 5. The lever rule was also applied to compute the SFE for supercells of size $n_s = 97$ and 113. The required runtimes for the different strategies of SFE determination for paramagnetic *fcc* Fe-N show a similar relative trend as for the calculations for non-magnetic *fcc* Fe-N, albeit at increased overall runtime (Fig. 7). The lever rule approach saves ~1/2 of computational resources for $n_i = 33$ and ~15% of computational resources for $n_i = 49$ with respect to conventional axial interaction model calculations.

3.4.3. AISI 304 austenitic stainless steel

To validate the lever rule in a complex higher-order alloy, the case of *fcc* AISI 304 with the base composition *Fe-18.1Cr-7.9Ni-1.1Mn-0.54Si wt%* (*Fe-19.1Cr-7.4Ni-1.1Mn-1.1Si at.%*) is considered. The lattice parameter a_0^s at room temperature as a function of nitrogen content y_N^s of the entire supercell was obtained following the relationship for *fcc* AISI316 by Hummelshøj et al. [53]:

$$a_0^s\left(y_N^s\right) = 3.5965 + 0.006029\, y_N^s\ [\text{Å}] \quad (6)$$

As for Fe, the c/a-ratio of 1.616 was obtained by relaxing the *hcp* cell with the AISI 304 base composition at the ground-state volume and was kept constant for all following calculations. The SFE obtained from the lever rule is compared with the validation dataset from the axial interaction model in Fig. 8 [40]. For an interstitial region of $n_i = 33$ the associated error is $\leq$1.6 $\mathrm{mJ.m}^{-2}$ and for a larger interstitial region of $n_i = 49$, it is $\leq$0.6 $\mathrm{mJ.m}^{-2}$. The lever rule also computed the SFE for supercells of size $n_s = 97$ and 113. Fig. 9 shows the overall runtime of the different approaches for SFE determination in paramagnetic N-alloyed *fcc* AISI 304. For $n_i = 33$ the lever rule saves ~45% of computational resources, whereas for $n_i = 49$ the method only saves ~11% of computational resources with respect to conventional axial interaction model calculations.

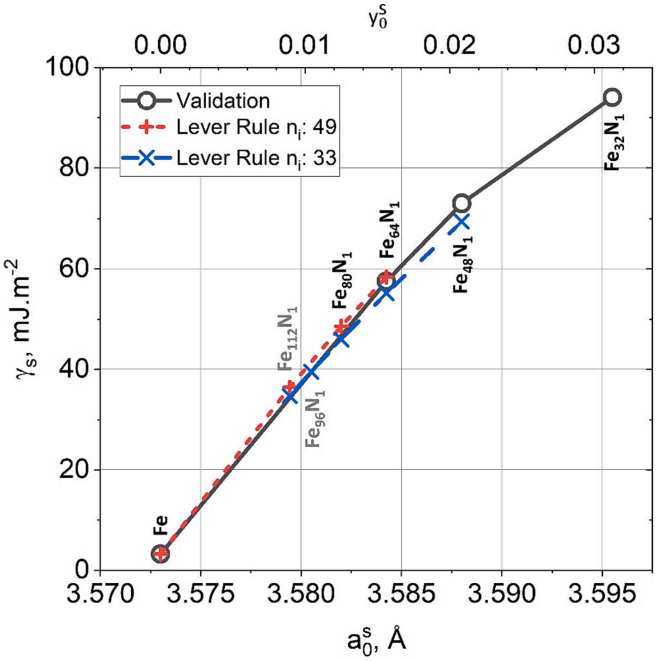

Fig. 6. SFE values of paramagnetic Fe-N obtained from the lever rule approach using $n_i = 33$ and $n_i = 49$ validated against the SFE obtained with the conventional axial interaction model on full supercells. The presented values include the magnetic entropy contribution to the SFE. The maximum discrepancy between the methods is 3.5 $\mathrm{mJ.m}^{-2}$ for $n_i = 33$ and 0.8 $\mathrm{mJ.m}^{-2}$ for $n_i = 49$. The lever rule furthermore obtained SFE values for larger supercells (shown in gray).

4. Application

4.1. Equidistant interstitial occupancy increments

A strong side of the presented lever rule approach is that it is not bound to the interstitial occupancies that are representable within supercells of (at the very best) 100–200 atoms. As the interstitial occupancy y tends to zero, the number of host-lattice atoms required to represent it tends to y^{-1}, i.e., infinity. As the lever rule is based on a linear combination of total energies from smaller supercells and primitive cells, it is not restricted in the representation of low interstitial occupancies. As any arbitrary interstitial occupancy up to a maximum of $y_{\max}^s = (n_i - 1)^{-1}$ can be represented (see Section 3.3), the approach conveniently allows mapping of the SFE at equidistant steps of the interstitial occupancy within this range. Given an equidistant point distribution in a smoothly developing SFE vs. N-content relationship, the feasibility of fitting across a reduced number of equidistantly spread points can be assessed with the ambition of further reducing required computational resources.

To demonstrate this, the nitrogen occupancy in AISI 304 was mapped in steps of $\Delta y_N = 0.0017$, corresponding to lattice parameter increments of $\Delta a_0 = 0.1$ pm. Fig. 10a shows the results from applying the lever rule in Equation (4) to determine the SFE values for *fcc* AISI 304 as a function of these increments in nitrogen content and its associated volume expansion. Both SFE values that consider and discard the effect of the magnetic entropy contribution F_{mag} from Equation (3) are plotted. The equidistant mapping of the SFE gives a smooth relationship and is in perfect agreement with values that were obtained using the conventional axial interaction model for SFE determination [40] (see green and cyan markers). The relationship was fitted with the polynomial $\gamma(a_0) = -689937 + 378016a_o - 51767a_o^2$ $\mathrm{mJ.m}^{-2}$, resulting in a high correlation with the SFE data reflected in a Pearson correlation coefficient of 0.99997 (Fig. 10b). Importantly, polynomial fits that were performed on gradually reduced SFE datasets resulted in an equally high correlation with the full dataset. Even for a reduction by a factor 5 to only 5 SFE values across the entire analyzed range of nitrogen content (uppermost, purple curve in Fig. 10b), the Pearson correlation coefficients was >0.99996. The introduced error by fitting drastically reduced datasets with respect to the unreduced original dataset was <1 $\mathrm{mJ.m}^{-2}$ (Fig. 10c). Therefore, the already reduced computational time made possible by the lever rule approach can be further reduced by SFE computation for a selective choice of few evenly spaced interstitial contents.

4.2. Multi-parameter SFE mapping

The presented data in Fig. 10 demonstrates that the lever rule approach is ideally suited for SFE mapping vs. interstitial content. Hitherto, such DFT-based analysis was limited to purely substitutional alloys [2,54]. Departing from the AISI 304 alloy considered in Section 3.4.3, we demonstrate that the efficiency of the developed method allows multi-parameter SFE mapping by efficiently computing the

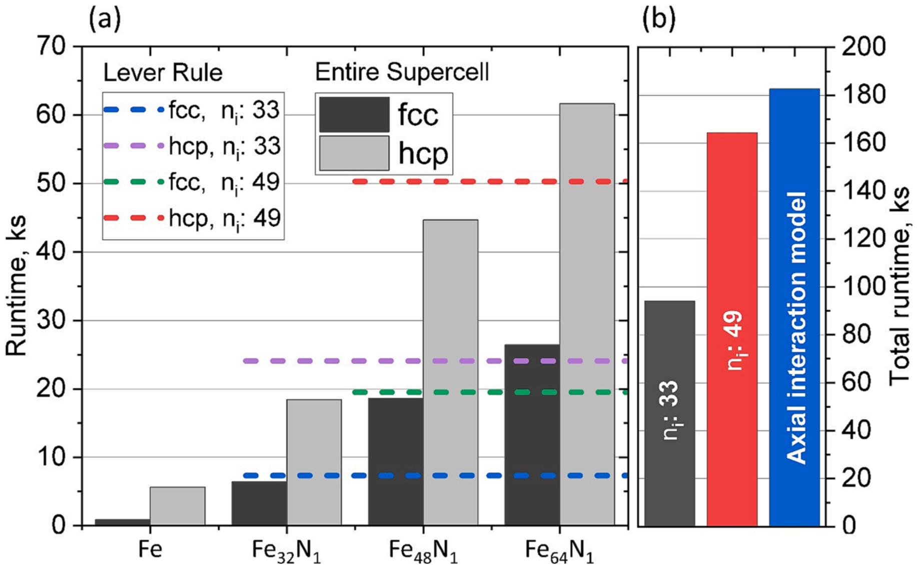

Fig. 7. (a) Runtime of the total energy calculations in paramagnetic fcc Fe-N in Fig. 4 of the full fcc and hcp supercells (gray bars) vs. the average runtime using the lever rule approach with $n_i = 33$ and $n_i = 49$. The total runtime for the 4 considered supercells in panel (b) shows that the lever rule approach saves ~1/2 of computational resources for $n_i = 33$ and ~15% of computational resources for $n_i = 49$.

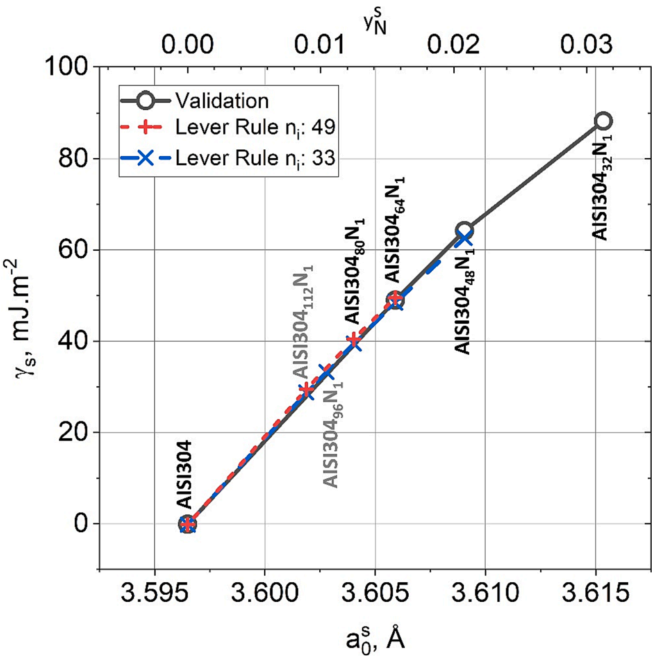

Fig. 8. SFE values of paramagnetic fcc AISI 304-N obtained from the lever rule approach using $n_i = 33$ and $n_i = 49$ validated against the SFE obtained with the conventional axial interaction model on full supercells. The presented values include the magnetic entropy contribution to the SFE. The maximum discrepancy between the methods is 1.6 mJ.m^{-2} for $n_i = 33$ and 0.6 mJ.m^{-2} for $n_i = 49$. The lever rule furthermore obtained SFE values for compositions associated with large supercells (shown in gray).

combined influences of N occupancy and Ni content on the SFE. Fig. 11 shows SFE values determined using Equation (4) and $n_i = 33$ for a nitrogen occupancy mapped in steps of $\Delta y^s_N = 0.0017$ and Ni content mapped in steps of $\Delta x_{Ni} = 0.5$ at.%. All ab initio parameters for calculating the SFE were kept identical to the calculations for AISI 304 in Section 4.1. Due to a lack of data on the combined effect of N and Ni on the lattice parameter at room temperature, only the significantly stronger effect of N on the volume V_s as reflected by Equation (6) is considered. The contours show that both N and Ni have a stabilizing effect on *fcc* relative to *hcp*. The stable-to-metastable transition is identified at 9.8 at.% Ni in the nitrogen-free condition, and at $y^s_N = 0.0045$ for the lowest considered Ni content of 3.4 at.%. The lever rule method reveals that nitrogen has a far stronger stabilizing effect on *fcc* than Ni, and that the stabilizing effect of Ni on *fcc* diminishes with increasing nitrogen content. As previously identified for different alloying elements in substitutional steel alloys [2,54], the effect of N and Ni alloying on the SFE does not obey simple addition, indicating that no universal composition equations for the SFE can be established. It is noted that the trend of increasing SFE with increasing Ni content is reported for ambient temperature. It was previously shown that this trend is inverted at elevated temperature [55].

5. Discussion

The presented lever rule approach approximates the total energy of a large supercell containing an interstitial by a balanced summation of the total energies of representative and smaller interstitial-containing and interstitial-free (bulk) supercells. The approach introduces negligible error with respect to the axial interaction model (Eq. (1)), extends the compositional space that can be analyzed and drastically improves computational performance and convergence behavior. It thus provides a new avenue for SFE-based materials design of alloys that contain interstitials to bridge the gap between efficient but flawed CALPHAD-based approaches and accurate but tedious and restricted conventional DFT-based approaches. The discussion mainly addresses the error margin and limitations of the developed method and draws up possible pathways for its future development and application.

5.1. Error assessment

The validation in Section 3.4 demonstrated that the underlying assumption of the lever rule approach is valid within an error margin of a few mJ.m^{-2} with respect to the conventional axial interaction model. Plotting the individual atomic energies of the $Fe_{64}N_1$ supercell (Fig. 5) revealed that defining the interstitial region with a supercell of 32 host-lattice atoms and 1 interstitial atom introduced an error which was associated with energy tails radiating from the octahedral region. The validation in Section 3.4 however demonstrated that these errors propagated to <4 mJ.m^{-2} error in SFE, often even half of that. While

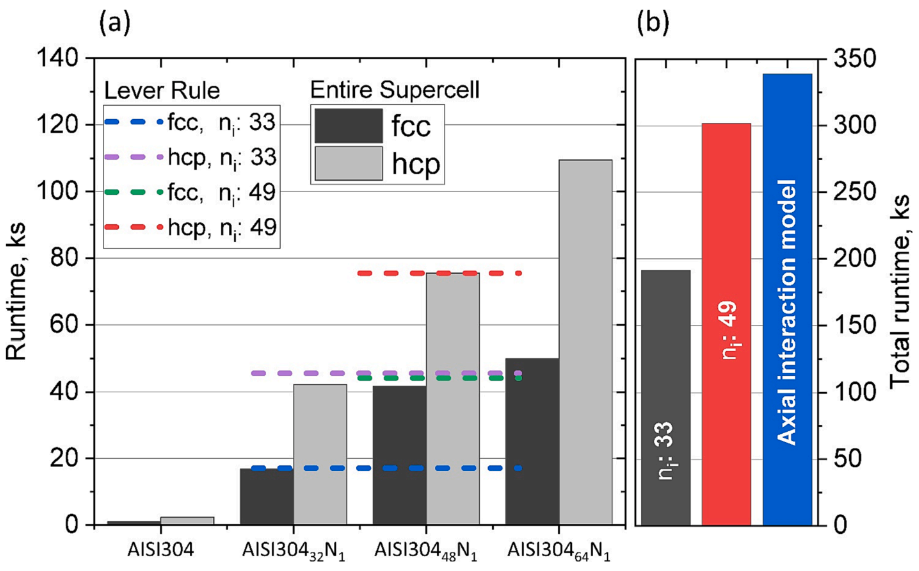

Fig. 9. (a) Runtime of the total energy calculations in paramagnetic fcc AISI 304 in Fig. 8 of the full fcc and hcp supercells (gray bars) vs. the average runtime using the lever rule approach with $n_i = 33$ and $n_i = 49$. The total runtime for the 4 considered supercells in panel (b) shows that the lever rule approach saves ~45% of computational resources for $n_i = 33$ and ~11% of computational resources for $n_i = 49$.

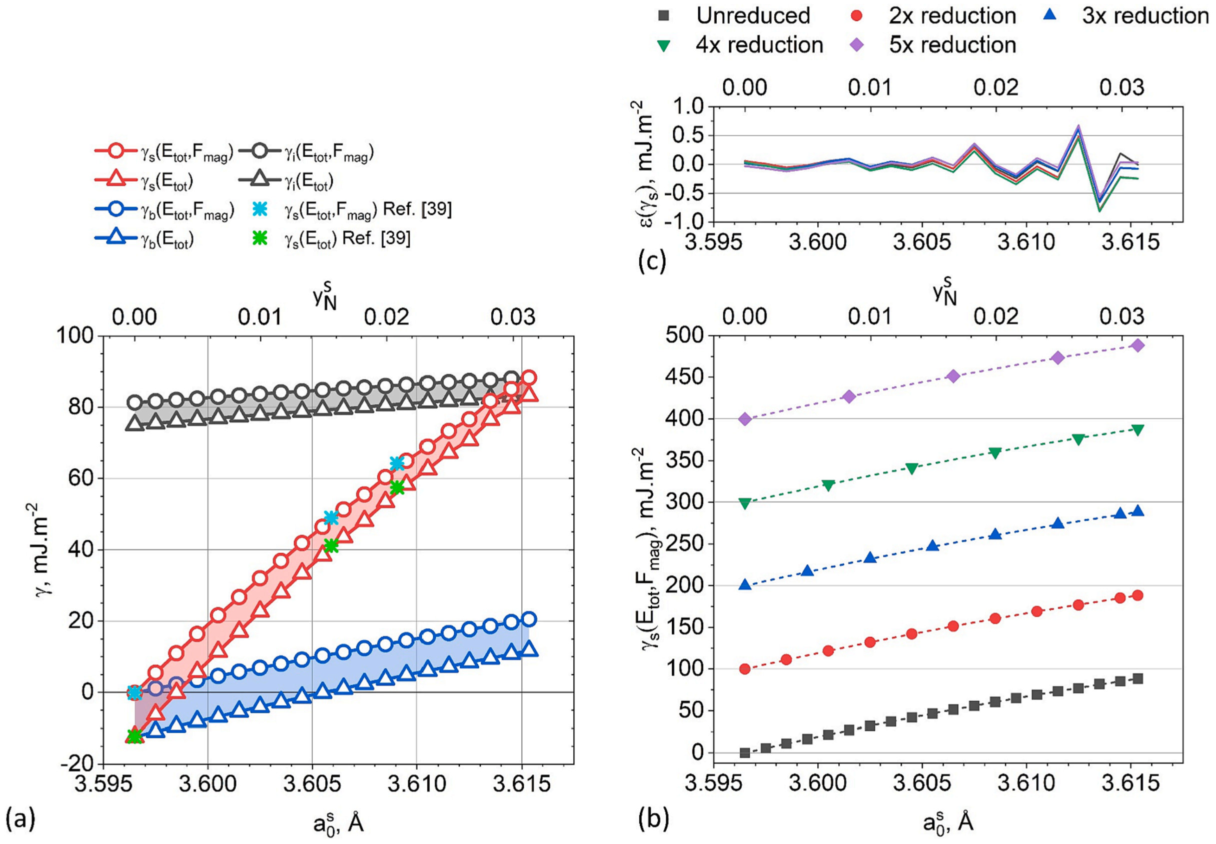

Fig. 10. (a) SFE values of paramagnetic fcc AISI304-N obtained from the lever rule approach in Equation (4) using $n_i = 33$. The computed SFE values for γ_i and γ_b as well as the resulting SFE value γ_s are plotted both with and without considering the magnetic entropy contribution F_{mag} from Eq. (3). The values are validated against values from conventional axial interaction model SFE calculations from Ref. [40] (see green and cyan markers). (b) Unreduced (black markers) and gradually reduced datasets and their respective 2nd order polynomial fits, offset by 100 mJ.m^{-2} steps for clarity. Panel (c) highlights the deviation $\varepsilon(\gamma_s)$ between the fitted SFE data from the different reduced datasets (dashed lines) and the unreduced SFE dataset (black markers). Even when reducing the dataset with a factor 5 the SFE is accurately described with <1 mJ.m^{-2} error by the respective applied 2nd order polynomial fits. All reduced datasets contained the SFE values for the lowest and highest nitrogen contents.

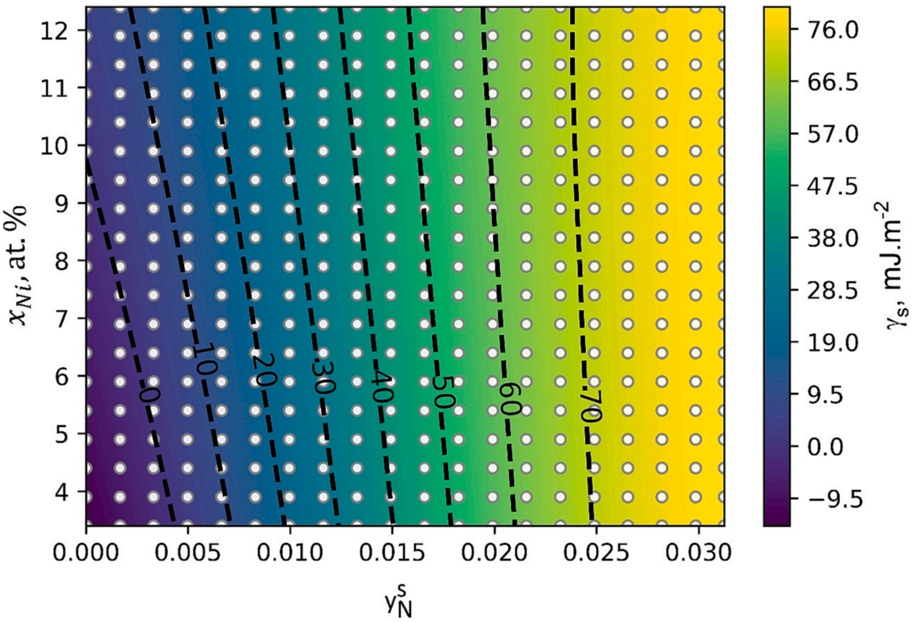

Fig. 11. SFE obtained using the lever rule with $n_i = 33$ as a function of nitrogen occupancy y_N^s and Ni content x_{Ni}. The markers indicate compositions where SFE values were calculated and the colormap represents interpolated values using a bivariate B-spline function. The SFE values are shown as average values of SFE values that consider the effect of the magnetic entropy contribution (Eq. (3)) and SFE values that neglect this contribution (see distinction in Fig. 10a). The dashed lines represent contours of constant SFE and indicate that both Ni and N alloying stabilize the fcc lattice. The stabilizing effect of Ni on the fcc lattice reduces with increasing N content.

most of the bulk region plotted in Fig. 5 had an approximately uniform atomic energy, as is characteristic for a homogeneous defect-free lattice, the uppermost plane of atoms revealed slightly reduced energy associated with nitrogen alloying. The same energy tail is not observable on the other end of the bulk region, which is due to the off-center position of the nitrogen atom within the $Fe_{32}N_1$ supercell that represents the interstitial region. The error can be reduced by choosing a larger interstitial region, for instance containing 48 host-lattice atoms instead of 32. The validation in this work highlighted that for most cases the slightly improved accuracy of <2 mJ.m^{-2} may not be worth the considerably increased computational workload.

It is furthermore encouraging that the error introduced on adopting the lever rule is largest for high interstitial contents, when the bulk region is comparably small and possible energy tails thus introduce a larger relative error. High interstitial contents are commonly represented with comparably small supercells, suitable for treatment with the conventional axial interaction model. In contrast, the lever rule approach is most effective for low interstitial contents that traditionally are associated with large supercells, which is also the application scenario for which the lever rule approach shows the highest accuarcy.

5.2. *Limitations and future perspective*

Following the presented hypothesis, validation and application examples, the proposed method may be applied for elucidating the combined effect of interstitial and substitutional alloying contents on the SFE. Given the robustness of calculating the total energy for reasonably sized supercells, the approach enables SFE-based development of alloys that contain interstitial elements. Obviously, this surpasses the limitations of current CALPHAD- and DFT-based approaches described in Section 1. The potential of the method for this application was highlighted in Section 4.2 by mapping the SFE in paramagnetic AISI 304 as a function of Ni and N content. The application of the lever rule approach in conjunction with EMTO is powerful as the CPA and DLM model allow the treatment of random solid solutions and paramagnetic alloys. A current limitation of EMTO is the lack of optimization-guided ionic relaxation, which limits the range in which interstitial compositions can be mapped. The applied manual ionic relaxation around the interstitial atom is tedious and was only carried out for one condition. While a slight deviation from such an optimized reference condition may be deemed acceptable, a large deviation could compromise the accuracy of results. A potential approach to address this limitation could be the consideration of DFT formalisms that allow for optimization-guided ionic relaxation to be applied in conjunction with the lever rule. For the analysis of multicomponent alloys, the randomness of the substitutional lattice would however need to be considered, for instance by the application of special quasi-random structures (SQS) [48], which might compromise the computational efficiency of the lever rule approach. The proposed method is therefore currently mostly limited by the complementary limitations of the different available DFT formalisms which may be overcome in the future.

6. Conclusion

This work introduces a new method for efficient SFE-mapping in complex dilute interstitial alloys using ab initio DFT. The method is designed towards application in SFE-based alloy design and it positions itself between efficient, but inaccurate, CALPHAD-based approaches and accurate, but tedious and restricted, traditional DFT-based approaches. The interstitial-affected and interstitial-free (bulk) regions of large interstitial-containing supercells are treated separately and their contributions to the overall SFE value are weighted with a lever rule approach. The main findings are:

- The lever rule approach led to an error of <4 mJ.m^{-2} in comparison with the conventional axial interaction model when validating on non-magnetic *fcc* Fe-N as well as paramagnetic *fcc* Fe-N and nitrogen-alloyed AISI 304 austenitic stainless steel.
- Using the lever rule approach, the computational resources with respect to the conventional axial interaction model could be drastically reduced.
- The lever rule approach makes SFE computation for traditionally unfeasible low interstitial contents accessible.

- In contrast to traditional methods, the proposed method allows mapping of the SFE with equidistant steps in interstitial content. A detailed analysis demonstrated that this allows a robust description of the SFE vs. interstitial content relationship with only few datapoints, associated with a further reduction in computational workload.
- The application of the lever rule approach was showcased by demonstrating SFE determination in paramagnetic AISI 304 austenitic stainless steel vs. tightly spaced nitrogen occupancies of the interstitial lattice. Moreover, the combined effect of N and Ni alloying on the DFT-based SFE was for the first time mapped in a 2-dimensional parameter space.
- N-alloying stabilized the *fcc* with respect to the *hcp* lattice more effectively than Ni-alloying. The stabilizing effect of Ni-alloying decreased with increased N content.

CRediT authorship contribution statement

Frank Niessen: Conceptualization, Methodology, Software, Validation, Writing – original draft, Writing – review & editing, Visualization. **Konstantin V. Werner:** Conceptualization, Methodology, Writing – review & editing. **Wei Li:** Software, Writing – review & editing. **Song Lu:** Software, Writing – review & editing. **Levente Vitos:** Software, Writing – review & editing, Supervision. **Matteo Villa:** Writing – review & editing, Supervision, Funding acquisition. **Marcel A.J. Somers:** Writing – review & editing, Supervision, Resources, Project administration, Funding acquisition.

Declaration of Competing Interest

The authors declare that they have no known competing financial interests or personal relationships that could have appeared to influence the work reported in this paper.

Data availability

No data was used for the research described in the article.

Acknowledgement

This work was supported by the Independent Research Fund Denmark as part of the project SFETailor (Grant No. 9041-00145B). The computation was performed using the Niflheim cluster at the Technical University of Denmark. S. Lu thanks the support within the project ''SuperFraMat'' by Vinnova and the Strategic Mobility grant by the Swedish Foundation for Strategic Research (SSF). L. Vitos acknowledges the Swedish Research Council (VR), SSF, VINOVA, the Swedish Foundation for International Cooperation in Research and Higher Education (STINT), the Hungarian Scientific Research Fund (OTKA 128229), and the Carl Tryggers Foundation for financial support.

References

[1] R.E. Schramm, R.P. Reed, Stacking fault energies of fcc fe-Ni alloys by x-ray diffraction line profile analysis, MTA 7 (1976) 359–363, https://doi.org/10.1007/BF02642831.
[2] L. Vitos, J.-O. Nilsson, B. Johansson, Alloying effects on the stacking fault energy in austenitic stainless steels from first-principles theory, Acta Mater. 54 (2006) 3821–3826, https://doi.org/10.1016/j.actamat.2006.04.013.
[3] T.-H. Lee, E. Shin, C.-S. Oh, H.-Y. Ha, S.-J. Kim, Correlation between stacking fault energy and deformation microstructure in high-interstitial-alloyed austenitic steels, Acta Mater. 58 (2010) 3173–3186, https://doi.org/10.1016/j.actamat.2010.01.056.
[4] S. Allain, J.-P. Chateau, O. Bouaziz, S. Migot, N. Guelton, Correlations between the calculated stacking fault energy and the plasticity mechanisms in Fe–Mn–C alloys, Mater. Sci. Eng. A 387–389 (2004) 158–162, https://doi.org/10.1016/j.msea.2004.01.059.
[5] D.V. Edmonds, K. He, F.C. Rizzo, B.C. De Cooman, D.K. Matlock, J.G. Speer, Quenching and partitioning martensite—a novel steel heat treatment, Mater. Sci. Eng. A 438–440 (2006) 25–34, https://doi.org/10.1016/j.msea.2006.02.133.
[6] E.H. Valente, V.K. Nadimpalli, T.L. Christiansen, D.B. Pedersen, M.A.J. Somers, In-situ interstitial alloying during laser powder bed fusion of AISI 316 for superior corrosion resistance, Additive Manufact. Lett. 1 (2021), 100006, https://doi.org/10.1016/j.addlet.2021.100006.
[7] T. Furuhara, S. Annaka, Y. Tomio, T. Maki, Superelasticity in Ti–10V–2Fe–3Al alloys with nitrogen addition, Mater. Sci. Eng. A 438–440 (2006) 825–829, https://doi.org/10.1016/j.msea.2006.02.084.
[8] B. Wang, C. Hong, G. Winther, T.L. Christiansen, M.A.J. Somers, Deformation mechanisms in meta-stable and nitrogen-stabilized austenitic stainless steel during severe surface deformation, Materialia 12 (2020), 100751, https://doi.org/10.1016/j.mtla.2020.100751.
[9] Z. Li, C.C. Tasan, H. Springer, B. Gault, D. Raabe, Interstitial atoms enable joint twinning and transformation induced plasticity in strong and ductile high-entropy alloys, Sci. Rep. 7 (2017) 40704, https://doi.org/10.1038/srep40704.
[10] P.J. Spencer, A brief history of CALPHAD, Calphad 32 (2008) 1–8, https://doi.org/10.1016/j.calphad.2007.10.001.
[11] U.R. Kattner, The thermodynamic modeling of multicomponent phase equilibria, JOM 49 (1997) 14–19, https://doi.org/10.1007/s11837-997-0024-5.
[12] P. Hohenberg, W. Kohn, Inhomogeneous electron gas, Phys. Rev. 136 (1964) B864–B871, https://doi.org/10.1103/PhysRev.136.B864.
[13] W. Kohn, L.J. Sham, Self-consistent equations including exchange and correlation effects, Phys. Rev. 140 (1965) A1133–A1138, https://doi.org/10.1103/PhysRev.140.A1133.
[14] S. Bigdeli, H. Ehtehsami, Q. Chen, H. Mao, P. Korzhavy, M. Selleby, New description of metastable hcp phase for unaries Fe and Mn: Coupling between first-principles calculations and CALPHAD modeling: New description of metastable hcp phase for unaries Fe and Mn, Phys. Status Solidi B 253 (2016) 1830–1836, https://doi.org/10.1002/pssb.201600096.
[15] S. Bigdeli, M. Selleby, A thermodynamic assessment of the binary Fe-Mn system for the third generation of Calphad databases, Calphad 64 (2019) 185–195, https://doi.org/10.1016/j.calphad.2018.11.011.
[16] O. Grässel, G. Frommeyer, C. Derder, H. Hofmann, Phase transformations and mechanical properties of Fe-Mn-Si-AlTRIP-steels, J. Phys. IV France. 07 (1997) C5-383–C5-388. 10.1051/jp4:1997560.
[17] A. Saeed-Akbari, J. Imlau, U. Prahl, W. Bleck, Derivation and variation in composition-dependent stacking fault energy maps based on subregular solution model in high-manganese steels, Metall. Mat. Trans. A 40 (2009) 3076–3090, https://doi.org/10.1007/s11661-009-0050-8.
[18] O.A. Zambrano, Stacking fault energy maps of Fe–Mn–Al–C–Si steels: effect of temperature, grain size, and variations in compositions, J. Eng. Mater. Technol. 138 (2016), 041010, https://doi.org/10.1115/1.4033632.
[19] D.T. Pierce, J.A. Jiménez, J. Bentley, D. Raabe, C. Oskay, J.E. Wittig, The influence of manganese content on the stacking fault and austenite/ε-martensite interfacial energies in Fe–Mn–(Al–Si) steels investigated by experiment and theory, Acta Mater. 68 (2014) 238–253, https://doi.org/10.1016/j.actamat.2014.01.001.
[20] X. Sun, S. Lu, R. Xie, X. An, W. Li, T. Zhang, C. Liang, X. Ding, Y. Wang, H. Zhang, L. Vitos, Can experiment determine the stacking fault energy of metastable alloys? Mater. Des. 199 (2021), 109396 https://doi.org/10.1016/j.matdes.2020.109396.
[21] K.V. Werner, F. Niessen, W. Li, S. Lu, L. Vitos, M. Villa, M.A.J. Somers, Reconciling experimental and theoretical stacking fault energies in face-centered cubic materials with the experimental twinning stress, Materialia 27 (2023), 101708, https://doi.org/10.1016/j.mtla.2023.101708.
[22] K.V. Werner, F. Niessen, M. Villa, M.A.J. Somers, Experimental validation of negative stacking fault energies in metastable face-centered cubic materials, Appl. Phys. Lett. 119 (2021).
[23] M. Shih, J. Miao, M. Mills, M. Ghazisaeidi, Stacking fault energy in concentrated alloys, Nat. Commun. 12 (2021) 3590, https://doi.org/10.1038/s41467-021-23860-z.
[24] S. Wei, C.C. Tasan, Deformation faulting in a metastable CoCrNiW complex concentrated alloy: a case of negative intrinsic stacking fault energy? Acta Mater. 200 (2020) 992–1007, https://doi.org/10.1016/j.actamat.2020.09.056.
[25] A. Abbasi, A. Dick, T. Hickel, J. Neugebauer, First-principles investigation of the effect of carbon on the stacking fault energy of Fe–C alloys, Acta Mater. 59 (2011) 3041–3048, https://doi.org/10.1016/j.actamat.2011.01.044.
[26] X. Wang, R.R. De Vecchis, C. Li, H. Zhang, X. Hu, S. Sridar, Y. Wang, W. Chen, W. Xiong, Design metastability in high-entropy alloys by tailoring unstable fault energies, Sci. Adv. 8 (2022) eabo7333, https://doi.org/10.1126/sciadv.abo7333.
[27] N.I. Medvedeva, M.S. Park, D.C. Van Aken, J.E. Medvedeva, First-principles study of Mn, Al and C distribution and their effect on stacking fault energies in fcc Fe, J. Alloy. Compd. 582 (2014) 475–482, https://doi.org/10.1016/j.jallcom.2013.08.089.
[28] Y. Su, S. Xu, I.J. Beyerlein, Density functional theory calculations of generalized stacking fault energy surfaces for eight face-centered cubic transition metals, J. Appl. Phys. 126 (2019), 105112, https://doi.org/10.1063/1.5115282.
[29] A. Dick, The Effect of Disorder on the Concentration-Dependence of Stacking Fault Energies in Fe1-xMnx – a First Principles Study, Steel Res. Int. (2009), https://doi.org/10.2374/SRI09SP015.
[30] R. Xie, S. Lu, W. Li, Y. Tian, L. Vitos, Dissociated dislocation-mediated carbon transport and diffusion in austenitic iron, Acta Mater. 191 (2020) 43–50, https://doi.org/10.1016/j.actamat.2020.03.042.
[31] S. Lu, R. Li, K. Kádas, H. Zhang, Y. Tian, S.K. Kwon, K. Kokko, Q.-M. Hu, S. Hertzman, L. Vitos, Stacking fault energy of C-alloyed steels: the effect of magnetism, Acta Mater. 122 (2017) 72–81, https://doi.org/10.1016/j.actamat.2016.09.038.
[32] T. Hickel, S. Sandlöbes, R.K.W. Marceau, A. Dick, I. Bleskov, J. Neugebauer, D. Raabe, Impact of nanodiffusion on the stacking fault energy in high-strength

steels, Acta Mater. 75 (2014) 147–155, https://doi.org/10.1016/j.actamat.2014.04.062.

[33] H.J. Bae, K.K. Ko, M. Ishtiaq, J.G. Kim, H. Sung, J.B. Seol, On the stacking fault forming probability and stacking fault energy in carbon-doped 17 at% Mn steels via transmission electron microscopy and atom probe tomography, J. Mater. Sci. Technol. 115 (2022) 177–188, https://doi.org/10.1016/j.jmst.2021.11.027.

[34] P.J.H. Denteneer, W. van Haeringen, Stacking-fault energies in semiconductors from first-principles calculations, J. Phys. C Solid State Phys. 20 (1987) L883–L887, https://doi.org/10.1088/0022-3719/20/32/001.

[35] C. Cheng, R.J. Needs, V. Heine, Inter-layer interactions and the origin of SiC polytypes, J. Phys. C Solid State Phys. 21 (1988) 1049–1063, https://doi.org/10.1088/0022-3719/21/6/012.

[36] U.K. Viswanathan, S. Banerjee, R. Krishnan, Effects of aging on the microstructure of 17–4 PH stainless steel, Mater. Sci. Eng. A 104 (1988) 181–189, https://doi.org/10.1016/0025-5416(88)90420-X.

[37] F. Niessen, M. Villa, F. Danoix, J. Hald, M.A.J. Somers, In-situ analysis of redistribution of carbon and nitrogen during tempering of low interstitial martensitic stainless steel, Scr. Mater. 154 (2018) 216–219, https://doi.org/10.1016/j.scriptamat.2018.06.004.

[38] F. Niessen, A.A. Gazder, J. Hald, M.A.J. Somers, Multiscale in-situ studies of strain-induced martensite formation in inter-critically annealed extra-low-carbon martensitic stainless steel, Acta Mater. 220 (2021), 117339, https://doi.org/10.1016/j.actamat.2021.117339.

[39] G. Krauss, Martensite in steel: strength and structure, Mater. Sci. Eng. A 273–275 (1999) 40–57, https://doi.org/10.1016/S0921-5093(99)00288-9.

[40] F. Niessen, W. Li, K.V. Werner, S. Lu, L. Vitos, M. Villa, M.A.J. Somers, Ab initio study of the effect of interstitial alloying on the intrinsic stacking fault energy of paramagnetic γ-Fe and austenitic stainless steel, Acta Mater. (2023), 118967, https://doi.org/10.1016/j.actamat.2023.118967.

[41] P. Soven, Coherent-potential model of substitutional disordered alloys, Phys. Rev. 156 (1967) 809–813, https://doi.org/10.1103/PhysRev.156.809.

[42] L. Vitos, I.A. Abrikosov, B. Johansson, Anisotropic lattice distortions in random alloys from first-principles theory, Phys. Rev. Lett. 87 (2001), 156401, https://doi.org/10.1103/PhysRevLett.87.156401.

[43] B.L. Gyorffy, A.J. Pindor, J. Staunton, G.M. Stocks, H. Winter, A first-principles theory of ferromagnetic phase transitions in metals, J. Phys. F 15 (1985) 1337–1386, https://doi.org/10.1088/0305-4608/15/6/018.

[44] S. Bigdeli, H. Mao, M. Selleby, On the third-generation Calphad databases: an updated description of Mn: On the third-generation Calphad databases, Phys. Status Solidi B 252 (2015) 2199–2208, https://doi.org/10.1002/pssb.201552203.

[45] Q. Chen, B. Sundman, Modeling of thermodynamic properties for Bcc, Fcc, liquid, and amorphous iron 22 (2001) 14.

[46] L. Vitos, Computational Quantum Mechanics for Materials Engineers: the EMTO Method and Applications, Springer, London, 2007.

[47] G. Grimvall, Spin disorder in paramagnetic fcc iron, Phys. Rev. B 39 (1989) 12300–12301, https://doi.org/10.1103/PhysRevB.39.12300.

[48] A. Zunger, S.-H. Wei, L.G. Ferreira, J.E. Bernard, Special quasirandom structures, Phys. Rev. Lett. 65 (1990) 353–356, https://doi.org/10.1103/PhysRevLett.65.353.

[49] C. Jiang, B.P. Uberuaga, Efficient *ab initio* modeling of random multicomponent alloys, Phys. Rev. Lett. 116 (2016), 105501, https://doi.org/10.1103/PhysRevLett.116.105501.

[50] L. Cheng, A. Böttger, T.H. de Keijser, E.J. Mittemeijer, Lattice parameters of iron-carbon and iron-nitrogen martensites and austenites, Scr. Metall. Mater. 24 (1990) 509–514, https://doi.org/10.1016/0956-716X(90)90192-J.

[51] S. Kibey, J.B. Liu, M.J. Curtis, D.D. Johnson, H. Sehitoglu, Effect of nitrogen on generalized stacking fault energy and stacking fault widths in high nitrogen steels, Acta Mater. 54 (2006) 2991–3001, https://doi.org/10.1016/j.actamat.2006.02.048.

[52] H. Gholizadeh, C. Draxl, P. Puschnig, The influence of interstitial carbon on the γ-surface in austenite, Acta Mater. 61 (2013) 341–349, https://doi.org/10.1016/j.actamat.2012.09.066.

[53] T.S. Hummelshøj, T.L. Christiansen, M.A.J. Somers, Lattice expansion of carbon-stabilized expanded austenite, Scr. Mater. 63 (2010) 761–763, https://doi.org/10.1016/j.scriptamat.2010.05.031.

[54] L. Vitos, P.A. Korzhavyi, J.-O. Nilsson, B. Johansson, Stacking fault energy and magnetism in austenitic stainless steels, Phys. Scr. 77 (2008), 065703, https://doi.org/10.1088/0031-8949/77/06/065703.

[55] Z. Dong, W. Li, G. Chai, L. Vitos, Strong temperature – dependence of Ni -alloying influence on the stacking fault energy in austenitic stainless steel, Scr. Mater. 178 (2020) 438–441, https://doi.org/10.1016/j.scriptamat.2019.12.013.